Materials Advances

PAPER

View Article Online
View Journal | View Issue

Cite this: *Mater. Adv.*, 2026, 7, 2752

Design of a MgO@EDTA@Ag nanocatalyst for sustainable synthesis of xanthene and rhodamine B degradation

Anamika Brahma,[a] Ankita Borah,[a] Masoume Malmir[b] and Snigdha Singh *[ac]

Received 23rd October 2025,
Accepted 9th January 2026

DOI: 10.1039/d5ma01226k

rsc.li/materials-advances

The development of efficient and sustainable catalysts is crucial for advancing green chemical processes and environmental remediation. In this study, a MgO@EDTA@Ag nanocomposite was synthesized and utilized as a multifunctional, heterogeneous catalyst for the environmentally sustainable synthesis of xanthene derivatives and the catalytic degradation of rhodamine B dye, both of which hold significant pharmaceutical and environmental relevance. EDTA immobilization enhanced surface coordination for Ag anchoring and promoted electron transfer and reactive species generation. The catalyst was characterised using techniques like XRD, XPS, FESEM, TEM, FTIR, EDAX, TGA, N_2 adsorption–desorption and BET analysis, confirming its structural integrity, morphology, thermal stability, and high surface area. The nanocomposite exhibited excellent catalytic efficiency, supported by favourable green chemistry metrics including an *E*-factor of 0.23, process mass intensity (PMI) of 1.23, reaction mass efficiency (RME) of 90.06%, and carbon efficiency (CE) of 90%. Its reusability and environmental compatibility further emphasize its potential for sustainable applications in chemical synthesis and wastewater treatment. In the photocatalytic degradation of rhodamine B dye, the catalyst achieved an excellent 96% degradation within one hour by using 0.02 mg nanocatalyst in 2 mL dye solution.

Introduction

Heterogeneous catalysts have attracted growing interest over the years due to their distinct advantages over homogeneous catalysts, including superior selectivity, ease of recovery, and excellent reusability in long-term processes.[1] Reactions involving heterogeneous catalysts are governed by variations in the free energy of chemical intermediates influenced by their interaction with the catalyst's solid surface.[2] The fundamental goal of catalysis research is to unravel these surfaces at the molecular and electronic levels, enabling precise prediction and control of catalytic activity.[3] Metal oxide nanoparticles have gained significant attention in the field of catalysis due to their unique physicochemical properties, including high surface area, tunable morphology, and active surface sites that enhance catalytic efficiency.[4,5] These advantages have positioned metal oxide nanoparticles as powerful tools in designing next-generation catalytic systems that align with the principles of green chemistry.[6] Their ability to promote reactions under milder conditions, minimize byproduct formation, and enable cleaner reaction profiles makes them valuable in industrial and pharmaceutical applications.[7,8]

Xanthenes and their derivatives represent a significant class of compounds with wide-ranging applications in both pharmaceutical and materials science, and can be synthesized efficiently using heterogeneous catalysts.[9] These oxygen-containing heterocyclic compounds possess a pyran ring, which is responsible for their diverse biological potential and chemical reactivity.[10] They show a wide range of biological activities, including antifungal,[11] anti-inflammatory,[12] antiphlogistic, anticonvulsant, anti-analgesic, antiplatelet, and antigenotoxic properties,[13] making them highly valuable for therapeutic application.[14] In addition to medicinal benefits, xanthene derivatives are utilized in the development of pH-sensitive fluorescent materials for biomolecular visualization, as well as in laser visualization and dye manufacturing.[15] Their structural versatility enables easy functionalization, allowing chemists to develop a wide variety of derivatives suited for specific biological and industrial purposes. This diverse utility underscores the continued interest in the synthesis of xanthene derivatives, especially through green and sustainable methods that align with modern environmental and economic goals.[16] Fig. 1 shows biologically active compounds containing the xanthene core structure, such as

---

[a] *Drug Discovery and Development Laboratory, Department of Chemistry, University of Delhi, Delhi-110007, India. E-mail: ssingh3@chemistry.du.ac.in*
[b] *Centre for Green Chemical Science, School of Chemical Sciences, University of Auckland, Auckland, New Zealand*
[c] *Institute for Nanomedical Sciences (INMS), University of Delhi, Delhi-110007, India*

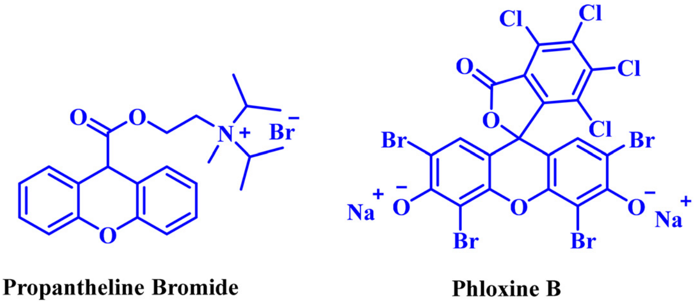

Fig. 1 Some important xanthene derivatives.

propantheline bromide, phloxine B, and methantheline bromide. Propantheline bromide is a quaternary ammonium anticholinergic agent that blocks muscarinic receptors, reducing gastrointestinal motility and gastric acid secretion. It is commonly used to manage peptic ulcers and irritable bowel syndrome.[17] Phloxine B is a halogenated xanthene dye with antimicrobial properties, effective against Gram-positive bacteria, and it is utilised in microbial viability assays and photodynamic studies.[18] Methantheline bromide is an anticholinergic agent that inhibits muscarinic receptors, leading to decreased gastric acid secretion and smooth muscle spasms. It is employed in the treatment of peptic ulcers and functional gastrointestinal disorders.[19]

Dyes such as rhodamine B, crystal violet, methylene blue, *etc.* pose serious environmental threats when discharged into water, causing carcinogenic effects and disrupting the reproductive systems of humans and aquatic life.[20] Dye-contaminated water is treated using various methods such as adsorption and photocatalytic degradation, which help to remove or break down the harmful dye molecules.[21] Metal oxide nanoparticles act as an effective photocatalyst by generating reactive species under light irradiation that breaks down harmful organic dyes into non-toxic compounds.[22] Similarly, Ag nanoparticles significantly increase dye degradation by promoting efficient charge separation through their surface plasmon resonance effect (SPR), which increases light absorption and reduces the recombination of photogenerated electron–hole pairs.[23]

In this study, we have reported the successful synthesis of the MgO@EDTA@Ag nanocomposite and its application as an efficient heterogeneous catalyst for the synthesis of xanthene derivatives as well as its application in the degradation of rhodamine B dye. The incorporation of EDTA enhances the surface coordination capability, while Ag nanoparticles facilitate superior electron transfer and the generation of reactive species, thereby contributing to the nanocomposite's remarkable catalytic and photocatalytic activity.[24] A comprehensive characterization was conducted utilizing techniques such as XRD, XPS, FESEM, TEM, FTIR, EDAX, TGA, and N_2 adsorption–desorption to analyse the structural, morphological, and surface properties of the catalyst. Furthermore, the inductively coupled plasma (ICP) analysis technique was used to calculate the leached metal ion concentration in the reaction. The MgO@EDTA@Ag nanocomposite demonstrated excellent performance in promoting xanthene formation and achieving rapid and high-efficiency dye degradation, showcasing its potential as a sustainable and multifunctional material in green chemistry and environmental remediation.

Synthesis and characterization of the MgO@EDTA@Ag nanocomposite

The synthesis of MgO nanoparticles involved a two-step process, starting with the precipitation of $Mg(OH)_2$ from $MgSO_4$ and NaOH, followed by calcination at 450 °C.[25] The MgO@EDTA@Ag nanocomposite was then prepared by dispersing MgO and EDTA in water using sonication, and then $AgNO_3$ was added to the solution and stirred for 2 h.[26] The schematic procedure for the synthesis of the MgO@EDTA@Ag nanocomposite is shown in Fig. 2.

PXRD

PXRD analysis was conducted to investigate the crystal structure and phases of the materials. Fig. 3 presents the diffraction pattern

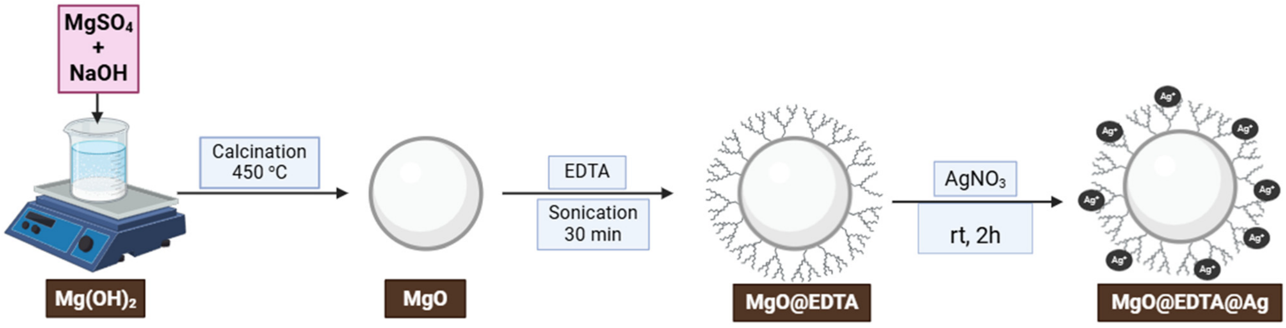

Fig. 2 Synthesis of MgO@EDTA@Ag nanocomposites.

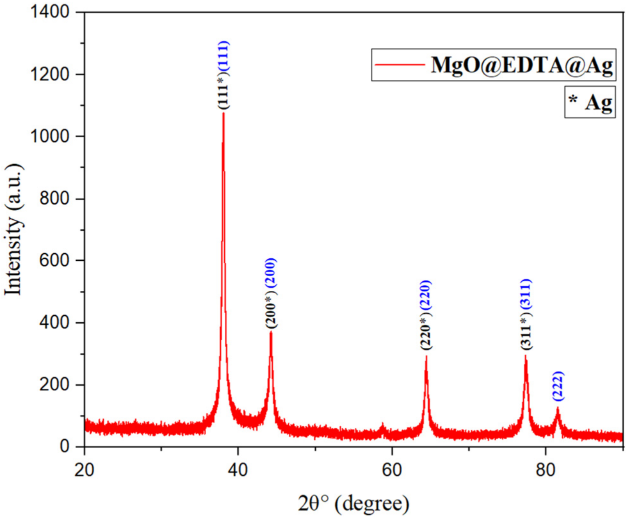

Fig. 3 XRD data of the synthesized MgO@EDTA@Ag nanocomposites.

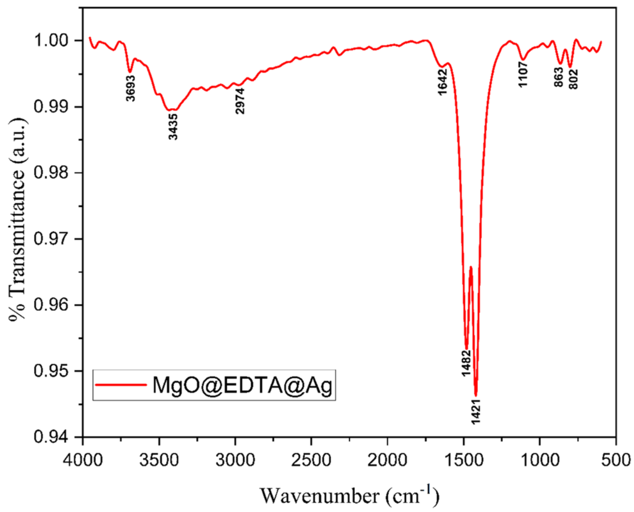

Fig. 4 FT-IR data of the synthesized MgO@EDTA@Ag nanocomposites.

of the synthesized MgO@EDTA@Ag nanocomposite. The diffraction peaks observed at 38°, 43.2°, 64°, 77.4°, and 80.1° in the MgO nanoparticles correspond to the crystal lattice planes (111), (200), (220), (311), and (222) (ICDD Card no: 00-004-0829).[27] The diffraction peaks align with the cubic phase of MgO, with slightly increased peak intensity and a shift towards higher 2θ values. The XRD profile of the pure MgO nanoparticles (Fig. S1) shows weak diffraction peaks at 38° (111) and 77.4° (311). After Ag deposition, these reflections become more intense because of the overlap with the characteristic peaks of Ag. The peaks observed at 38° (111), 43.2° (200), 64° (220), and 77.4° (311) correspond to the crystal lattice planes of the Ag nanoparticles (ICDD Card no: 00-001-1167).[28]

FT-IR

FT-IR spectroscopy was performed to confirm the successful immobilization of various groups over the synthesized nanoparticle (Fig. 4). The twin peak at 802 cm^{-1} is attributed to Mg–O vibration of the bulk MgO. Absorption peaks appearing at 1421 cm^{-1} and 1482 cm^{-1} indicate the vibrations of surface hydroxyl groups of MgO.[29] The immobilization of the EDTA over the MgO surface was confirmed by the characteristic bands observed at 2974 cm^{-1}, 1642 cm^{-1}, and 1107 cm^{-1}, corresponding to C–H stretching, C═O stretching, and aliphatic C–N stretching, respectively.[30] Additionally, the peaks observed at 3435 cm^{-1} and 3693 cm^{-1} are attributed to the –OH stretching vibration of the EDTA molecule.[31]

TGA

Thermogravimetric analysis shows that the initial weight loss of approximately 11% occurs below 300 °C, ascribed to the loss of water molecules (Fig. 5). There's a significant weight loss of 21% observed between 300 °C and 440 °C, corresponding to the decomposition of EDTA. Based on this weight loss, the experimental EDTA loading is estimated to be ∼21%, which is in close agreement with the theoretical value of ∼23% calculated from the synthesis stoichiometry, indicating efficient immobilisation of EDTA onto the MgO nanoparticles.

In the DTA curve, both exothermic and endothermic peaks were observed as shown in Fig. 5b. The exothermic peaks observed at 90 °C and 140 °C are gradual and correspond to the desorption of water molecules. The very strong endothermic peak observed at 370 °C is attributed to the decomposition of EDTA present in the synthesized nanocomposite.

BET

Fig. 6 depicts the adsorption–desorption isotherms of N_2 adsorption at 70.35 K on the MgO@EDTA@Ag nanoparticles. According to IUPAC, the adsorption isotherm is classified as type IV. The gap between adsorption (red curve) and desorption (black curve) signifies the presence of mesopores and pore connectivity. Brunauer–Emmett–Teller (BET) analysis is employed to determine the pore size distribution, which indicates that MgO@EDTA@Ag nanoparticles exhibit a bimodal pore distribution, indicating the coexistence of smaller and larger mesopores. While smaller pores provide a high density of active sites, larger pores facilitate efficient mass transfer, collectively contributing to improved catalytic efficiency. This behaviour can be attributed to the incorporation of Ag nanoparticles over MgO,[32] which contain mesopores with an average surface area of 30.958 $\text{m}^2\ \text{g}^{-1}$, a pore volume of 0.037 cc g^{-1}, and a diameter of 38.29 Å.

TEM

The histogram data, as shown in Fig. 7a, present the particle size distribution, signifying an average size of 20 nm. Transmission electron microscopy (TEM) images in Fig. 7b–e indicate the regular distribution with consistent size and morphology. The selected area electron diffraction (SAED) pattern, as depicted in Fig. 7f, provides structural insights through distinct diffraction rings with d-spacing values of 2.5 Å, 2.15 Å, 1.5 Å, 1.3 Å, and 1.2 Å corresponding to the planes (111), (200), (220), (311), and (222).[33]

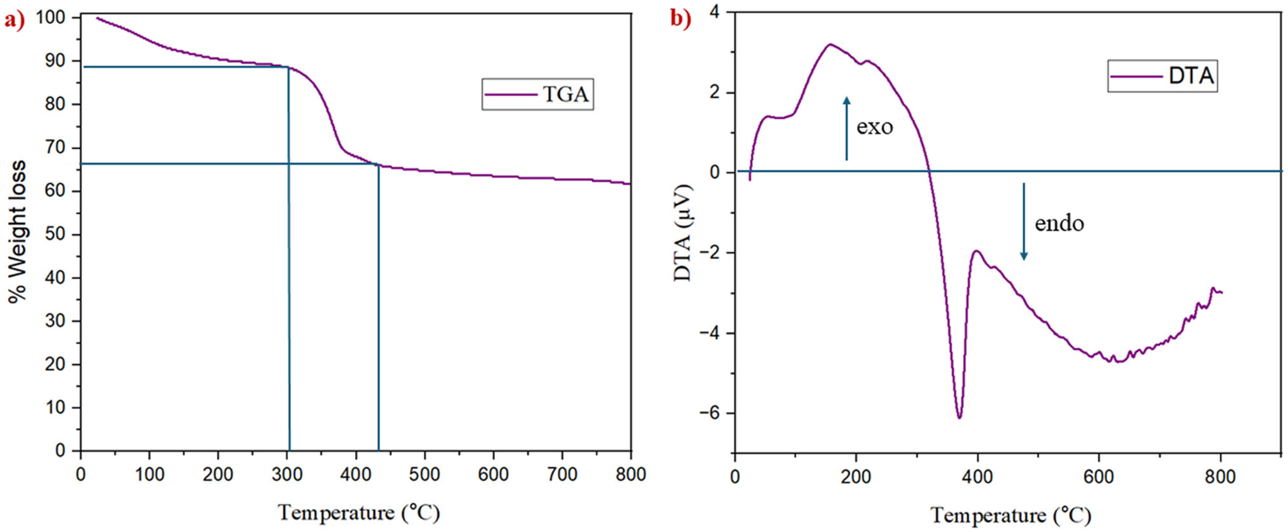

Fig. 5 (a) TGA and (b) DTA data of the synthesized MgO@EDTA@Ag nanocomposites.

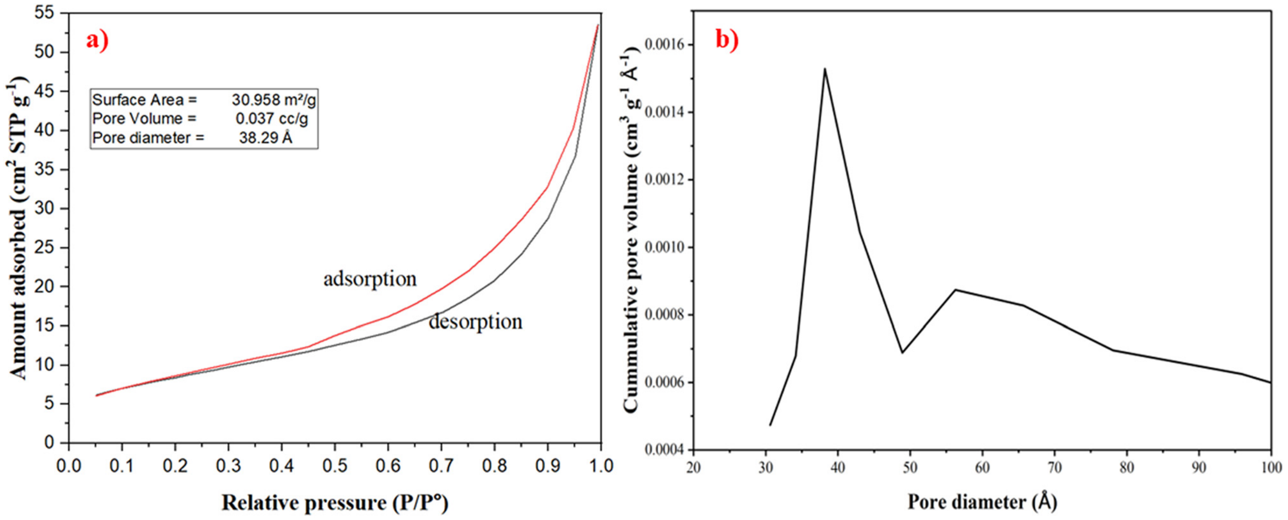

Fig. 6 (a) Nitrogen adsorption–desorption isotherms and (b) pore diameter of the MgO@EDTA@Ag nanocomposites.

EDAX

Fig. 8 reveals the energy dispersive X-ray analysis (EDAX) spectra of the synthesized nanocomposite that clearly show the immobilization of Ag over MgO@EDTA, and the percentage compositions of silver, magnesium, carbon, nitrogen, and oxygen are 44.68, 22.95, 2.28, 0.34, and 29.71 weight%, respectively along with the Pt peak at 2.1, which is present due to Pt used in the FESEM sample preparation as a conducting material.

XPS

X-Ray photoelectron spectroscopy (XPS) data, as shown in Fig. 9, discloses the chemical and elemental composition of a material's surface. The binding energy peak located at 1303 eV is attributed to magnesium in the +2 oxidation state, while the peak at 531 eV corresponds to oxygen species; in addition, the signals observed at 248 eV and 290 eV are assigned to carbon,[34] and the peaks appearing at 399.5 eV and 400 eV are characteristic of nitrogen-containing species. Silver shows the binding energy peak at 367.6 eV and 373.6 eV corresponding to $3d_{5/2}$ and $3d_{3/2}$, respectively, confirming the presence of silver in the +1 oxidation state.[35,36]

FESEM

The FESEM images of the MgO@EDTA@Ag nanocomposites reveal a flaky morphology characteristic of MgO nanoparticles with uniformly distributed spherical Ag nanoparticles observed on their surface (Fig. 10). This distinct contrast in morphology confirms the successful deposition of Ag nanoparticles onto the MgO@EDTA framework. Moreover, the dispersion of Ag

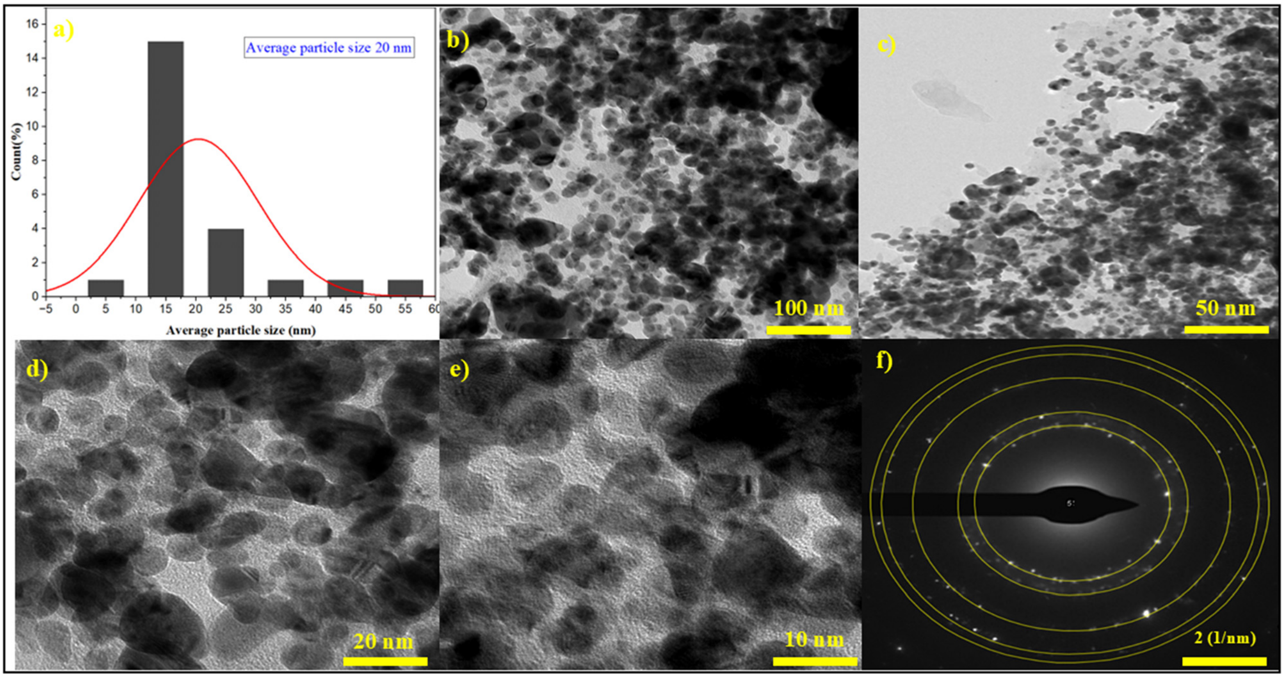

Fig. 7 (a) Histogram, (b)–(e) TEM image at varying sizes and (f) SAED data of the synthesized MgO@EDTA@Ag nanocomposites.

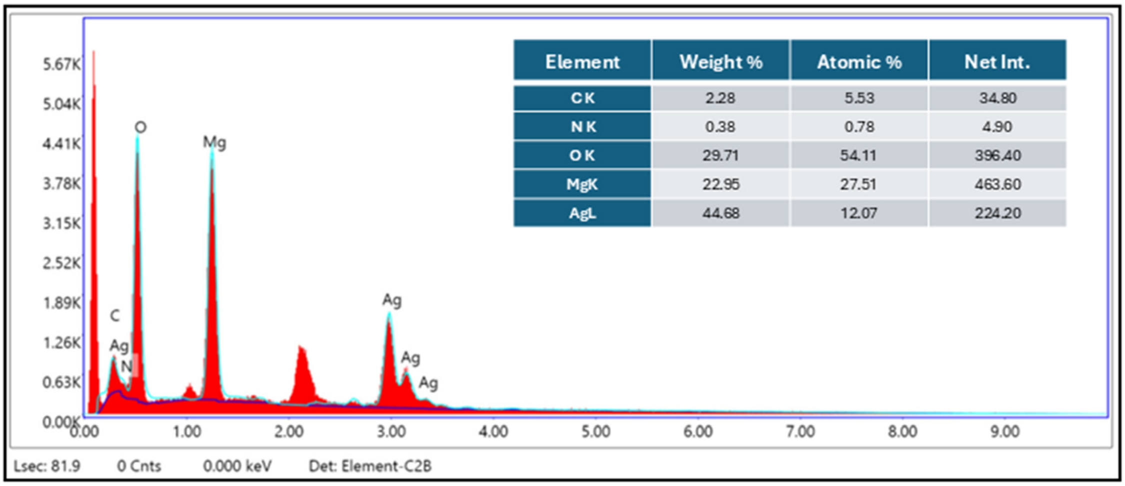

Element	Weight %	Atomic %	Net Int.
C K	2.28	5.53	34.80
N K	0.38	0.78	4.90
O K	29.71	54.11	396.40
MgK	22.95	27.51	463.60
AgL	44.68	12.07	224.20

Fig. 8 EDAX data of the synthesized MgO@EDTA@Ag nanocomposites.

correlates well with the BET results, which indicate mesoporosity and a bimodal pore distribution arising from partial pore blockage and surface modification.

Fig. 11 presents the Tauc plot $(\alpha h\nu)^{1/2}(\text{eV cm}^{-1})^{1/2}$ *versus* photon energy ($h\nu$) for MgO@EDTA@Ag, derived from UV-Vis-NIR diffuse reflectance data using the Kubelka–Munk function in the Tauc relation. The linear fitting of the absorption edges indicates an indirect optical transition. Extrapolation of the linear regions to the energy axis yields two optical band gap values of approximately 2.14 eV and 3.15 eV, suggesting the presence of multiple optical transitions in the material. Such behavior is commonly observed in composite or modified oxide systems, where structural modification or secondary phases influence the absorption characteristics.

Viability of the MgO@EDTA@Ag nanocomposite as a catalyst

The catalytic properties of the MgO@EDTA@Ag nanoparticles have been studied by synthesizing the xanthene moiety using 1,3-diketone and benzaldehyde under neat conditions at 80 °C. The optimization of the reaction was carried out using dimedone and benzaldehyde as the model substrates for synthesizing the desired xanthene derivative (**3a**). The catalytic performance of MgO@EDTA@Ag was compared by carrying out the reaction in the presence of MgO and $AgNO_3$, which shows a decrease in the

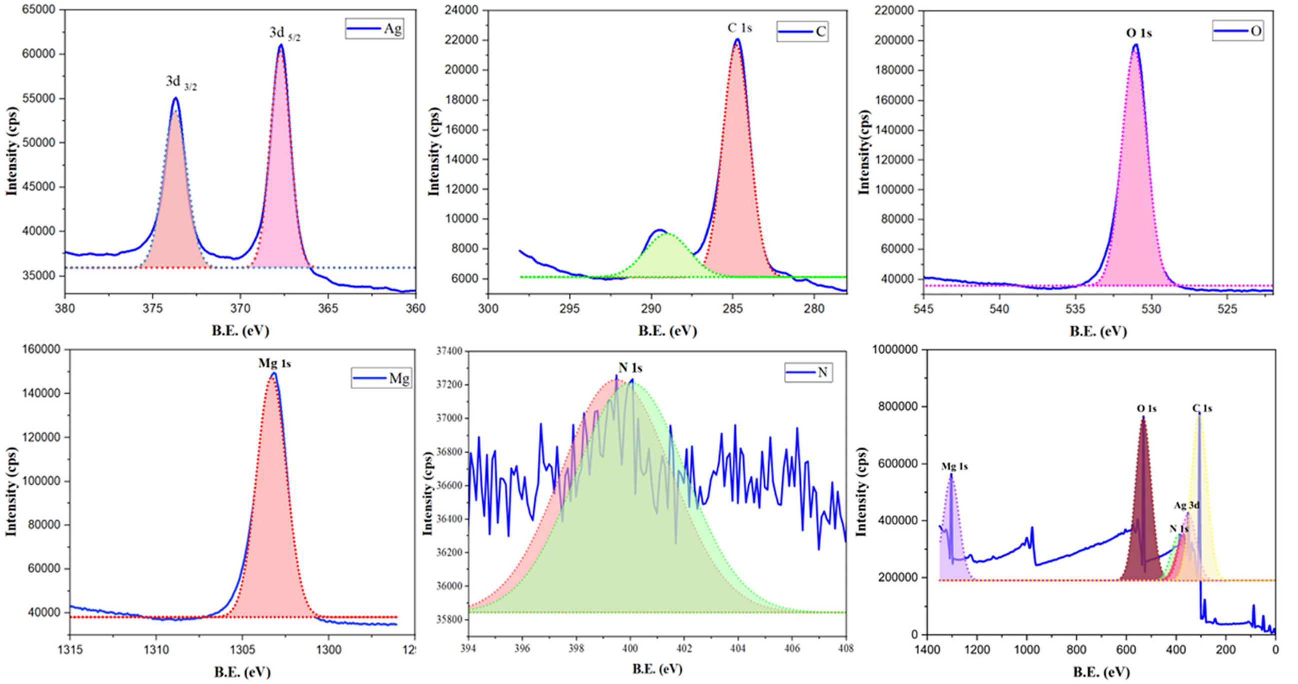

Fig. 9 XPS data of the synthesized MgO@EDTA@Ag nanocomposites.

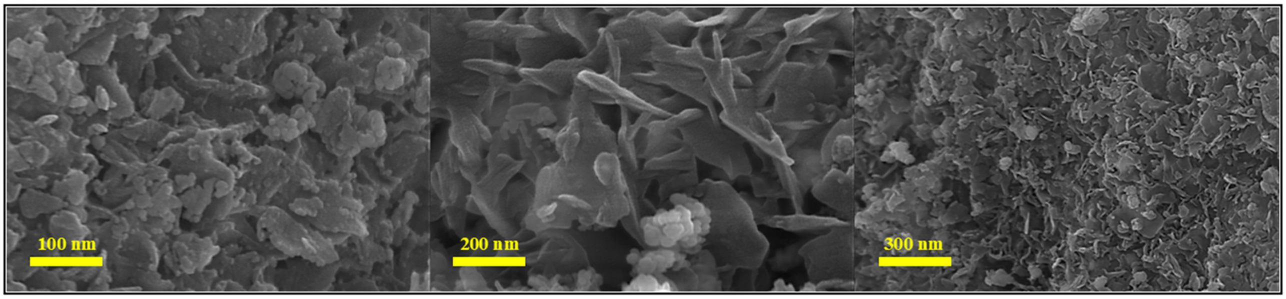

Fig. 10 FESEM images of the synthesized MgO@EDTA@Ag nanocomposites.

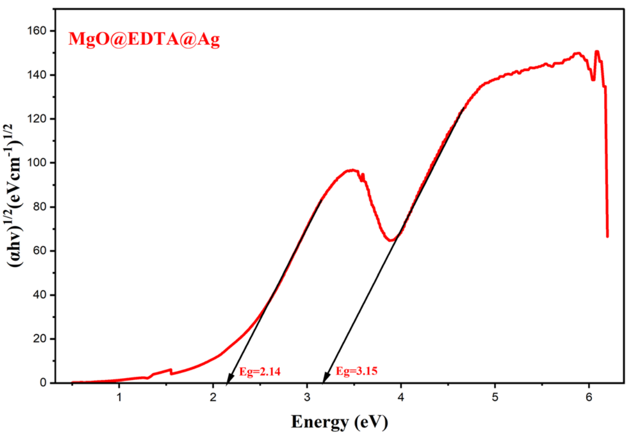

Fig. 11 Tauc's plots with the vertical axis scale starting from the origin for the synthesized MgO@EDTA@Ag nanocomposites.

% yield of the product (Table 1, entries 1 and 2). We studied the effects of different parameters on the reaction, like solvent effect, thermodynamic effect, and kinetic effect. It was observed that in the presence of green solvents like EtOH, H_2O, *etc.* (Table 1, entries 3 and 4), the reaction time was longer while the product yield was decreased. The reaction was conducted both without a catalyst at 80 °C and in the presence of a catalyst at room temperature, resulting in a reduced yield while taking a longer time to complete the reaction (Table 1, entries 5 and 6). In the presence of organic solvents like toluene, DMF, DMSO, and acetonitrile, an increase in reaction time and a decrease in the yield of product were observed (Table 1, entries 7–9). The thermodynamic effect on the reaction was studied by varying the reaction temperature. It was observed that a decrease in the reaction temperature increases the reaction time, while increasing the temperature above 80 °C shows no such effects on the time or yield of the reaction (Table 1, entry 10). A decrease in catalyst loading decreases the %yield of the reaction (Table 1, entry 11),

Table 1 Optimized synthesis of **3a** using the MgO@EDTA@Ag nanocomposite as a catalyst

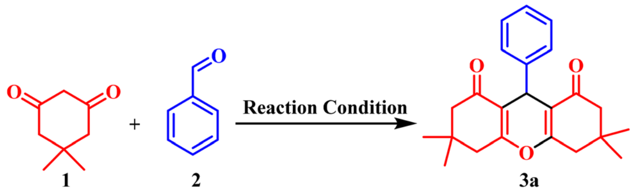

S. no.	Catalyst (mg)	Solvent[a]	Temp. (°C)	Time (min)	Yield[b] (%)
1	$AgNO_3$ (10)	—	80	45	72
2	MgO (10)	—	80	120	70.6
3	MgO@EDTA@Ag (10)	EtOH	80	105	46
4	MgO@EDTA@Ag (10)	H_2O	80	90	57
5	Without catalyst	—	80	180	55
6	MgO@EDTA@Ag (10)	—	RT	180	71
7	MgO@EDTA@Ag (10)	DMF	80	120	44
8	MgO@EDTA@Ag (10)	DMSO	80	120	39
9	MgO@EDTA@Ag (10)	Toluene	80	120	35
10	MgO@EDTA@Ag (10)	—	110	15	89
11	MgO@EDTA@Ag (5)	—	80	30	78
12	MgO@EDTA@Ag (20)	—	80	15	90
13	MgO@EDTA (10)	—	80	105	63
14	**MgO@EDTA@Ag (10)**	**—**	**80**	**15**	**90**

Reaction conditions: a mixture of benzaldehyde (0.5 mmol), dimedone (1 mmol), and MgO@EDTA@Ag (10 mg), in a solvent (2 mL) or under neat conditions was stirred at the required temperature. [a] Solvent (2 mL) or under neat conditions. [b] Isolated yields.

while an increase in catalyst loading shows no effect on the %yield of the product (Table 1, entry 12). Finally, the optimized conditions were found to be 10 mg of catalyst under neat conditions at 80 °C for 15 min (Table 1, entry 14). After achieving the optimized conditions, a wide substrate scope for MgO@EDTA@Ag nanocomposite-synthesized xanthene was demonstrated (Table 2).

The generality of the MgO@EDTA@Ag-catalyzed protocol was investigated using a wide range of aromatic aldehydes under solvent-free conditions at 80 °C. Aldehydes containing electron-donating groups ($-CH_3$, $-OCH_3$, $-OH$) as well as electron-withdrawing groups ($-NO_2$, $-Cl$, $-Br$) at various positions on the aromatic ring underwent smooth transformation to afford the corresponding xanthene derivatives (**3a–3j**) in moderate to excellent yields. Notably, halogenated substrates were well tolerated without any noticeable deactivation of the catalyst, indicating good functional group compatibility.

Furthermore, phenolic substrates such as resorcinol efficiently participated in the reaction, furnishing the corresponding bis-aryl xanthene derivatives (**3k–3l**) in good yields. The successful incorporation of resorcinol demonstrates the applicability of this methodology to polyhydroxy aromatic systems. Overall, the reaction scope highlights the robustness, versatility, and electronic insensitivity of the MgO@EDTA@Ag nanocatalyst for the synthesis of structurally diverse xanthene frameworks.

Gram scale reaction

After optimising the reaction at the laboratory scale, the synthesis of 3,3,6,6-tetramethyl-9-phenyl-3,4,5,6,7,9-hexahydro-1*H*-xanthene-1,8(2*H*)-dione (**3a**) was further performed on a gram scale to evaluate the practical applicability of the protocol (Scheme 1). The scale-up afforded 1.53 g of the compound (**3a**) with a yield of 87%, which is comparable to the 90% yield obtained on a small scale, demonstrating the robustness and scalability of the developed method.

Proposed mechanism for the synthesis of xanthene using the MgO@EDTA@Ag nanocomposite as a catalyst

A plausible mechanism for MgO@EDTA@Ag nanocatalyzed synthesis of xanthene is shown in Fig. 12. In the initial step, the aromatic aldehyde is activated through coordination of its carbonyl oxygen to the Lewis acidic Ag^+ sites, which enhances the electrophilicity of the carbonyl carbon and facilitates nucleophilic attack by the enolized β-diketone.[37] Concurrently, the basic sites of MgO promote enolization and proton transfer, enabling the formation of intermediate F *via* a Knoevenagel condensation.[38]

A second molecule of β-diketone is then similarly activated and adds to the intermediate F leading to the formation of new adduct G. Subsequent intramolecular cyclization and dehydration steps, facilitated by Lewis acid and basic sites present in the MgO@EDTA@Ag nanocomposite, yield the final xanthene product I. The catalyst plays a crucial dual role where Ag^+ activates the carbonyl groups[39] while MgO provides basic sites to promote enolization and proton transfer efficiently.[40] Throughout the reaction, Ag^+ retains its oxidation state (+1) and does not undergo reduction or leaching, indicating that the reaction proceeds *via* a heterogeneously catalyzed, non-redox pathway.

Experimental section

Synthesis of MgO

MgO nanoparticles were synthesized using a two-step method. In the first step, $Mg(OH)_2$ was prepared by adding 4.8 g of $MgSO_4{\cdot}6H_2O$ to 30 mL water and stirring the solution for 30 minutes. Then, a solution of NaOH was prepared by adding 0.4 g of NaOH to 10 mL water, and added dropwise to the mixture until the pH reached 10. The solution was stirred for an additional hour, followed by drying in an oven at 60 °C overnight. After drying, the synthesized $Mg(OH)_2$ was calcined at 450 °C for 4 h.[41]

$$\text{Step I: } MgSO_4 + 2NaOH \rightarrow Mg(OH)_2 + Na_2SO_4$$

$$\text{Step II: } Mg(OH)_2 \xrightarrow[450\,^{\circ}C]{\text{Calcination}} MgO$$

Facile fabrication of the MgO@EDTA@Ag nanocomposite

MgO nanoparticles (1 g, 1 eq.), and disodium ethylenediamine tetraacetic acid (EDTA) (1 g, 1 eq.), were dispersed in 100 mL of water using a sonicator for 30 minutes.[42] Then, to the solution, $AgNO_3$ (1 g, 1 eq.), was added and stirred for an additional 2 h. The resulting MgO@EDTA@Ag was washed multiple times with deionized water and then dried overnight at 60 °C.[43]

Synthesis of 3,3,6,6-tetramethyl-9-phenyl-3,4,5,6,7,9-hexahydro-1*H*-xanthene-1,8(2*H*)-dione (3a)

Dimedone (0.280 g, 2 eq.), benzaldehyde (0.1 mL, 1 eq.), and MgO@EDTA@Ag (10 mg) were added to a dry round-bottom flask.

Then the mixture was stirred neat at 80 °C for 15 minutes, and the progress was monitored by using TLC. Once the reactants were fully consumed, ethanol was added to the mixture, and the catalyst was isolated by centrifugation. The catalyst was

Table 2 Efficient preparation of xanthene derivatives using the MgO@EDTA@Ag nanocomposite as a catalyst

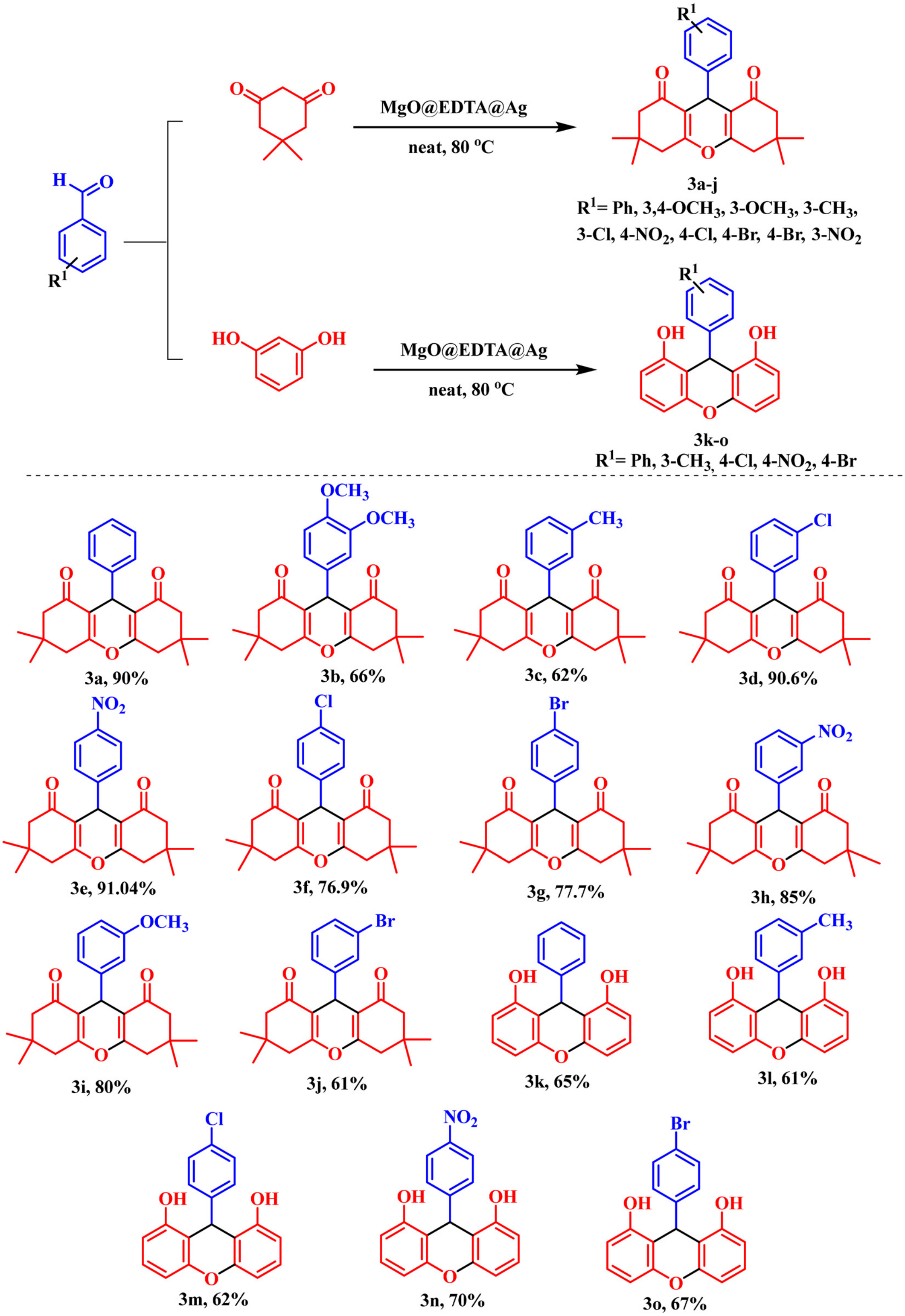

Reaction conditions: benzaldehydes (0.5 mmol), diketones (1 mmol) or resorcinol (1 mmol), MgO@EDTA@Ag (10 mg) were stirred under neat conditions at 80 °C.

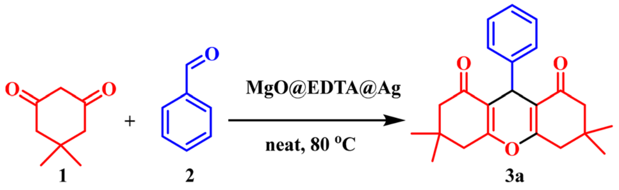

Scheme 1 Gram-scale synthesis of **3a**. Reaction conditions: a mixture of benzaldehyde (5 mmol), dimedone (10 mmol), and MgO@EDTA@Ag (100 mg), under neat conditions was stirred at 80 °C.

rinsed multiple times using ethanol and dried in an oven. The reaction mixture was dried and then quenched by adding ethyl acetate and sodium bisulphate solution to repeatedly extract and remove benzaldehyde. The organic layer was collected and dried.[44]

Evaluation of recyclability and green metrics for MgO@EDTA@Ag

The recyclability of MgO@EDTA@Ag was evaluated over six consecutive cycles under optimized conditions (5 mmol). The results demonstrated that the catalyst retained its catalytic efficiency throughout the cycles (Fig. 13). Furthermore, the PXRD and SEM analysis of the recycled catalyst confirmed its structural stability and integrity (Fig. S2 and S3).

To evaluate the role of the catalyst in xanthene synthesis, a hot filtration test was carried out. The reaction was initiated

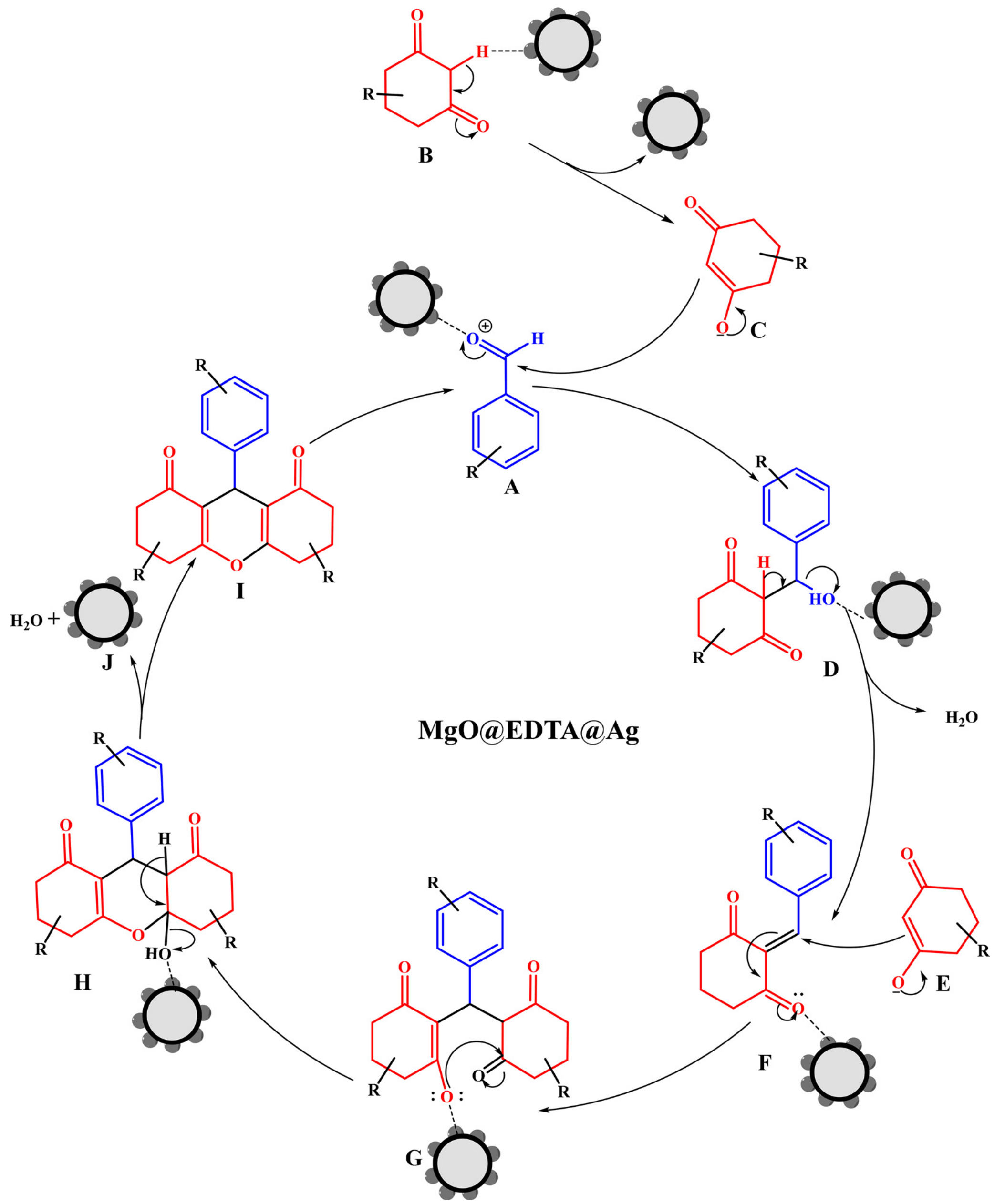

Fig. 12 Plausible mechanism of the synthesis of xanthene using the MgO@EDTA@Ag nanocomposite as a catalyst.

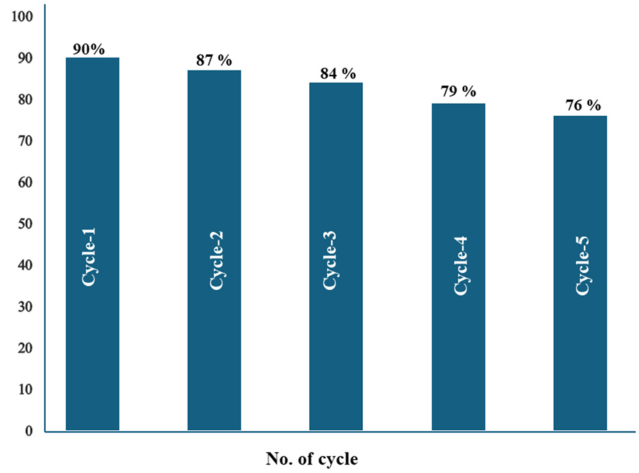

Fig. 13 Recyclability of the MgO@EDTA@Ag nanocomposite for the synthesis of **3a**.

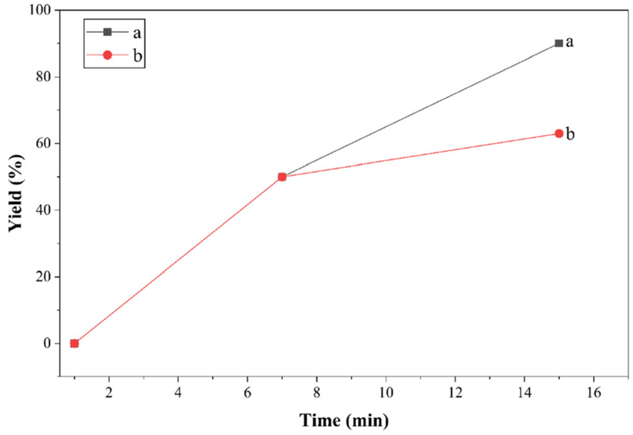

Fig. 14 (a) Synthesis of **3a** using the MgO@EDTA@Ag catalyst and (b) after the catalyst was separated from the reaction.[45,46]

under standard conditions, and after about five minutes, the TLC was monitored, which indicated roughly 50% product formation. The mixture was quickly filtered out while still hot to remove the catalyst. The clear filtrate was allowed to continue reacting under the same conditions for 15 min. Throughout the process, the reaction was monitored by TLC. The final yield of the product was found to be less than the expected yield, showing the importance of the catalyst throughout the reaction (Fig. 14).

The ICP analysis confirms minimal leaching of metals, with only trace amounts of Ag and Mg metals (Fig. S4) with the values 0.0011 ppm and 10.969 ppm, respectively, which are considered non-toxic and environmentally benign.[47]

Green chemistry metrics

To further demonstrate the environmental friendliness and sustainability of the xanthene synthesis catalysed by MgO@EDTA@Ag nanoparticles, green chemistry metrics were evaluated. These metrics, including atom economy (AE), reaction mass efficiency (RME), and *E*-factor, provide quantitative measures of how efficiently reactants are converted into the desired product and the extent of waste generated. The calculated values indicate that the reaction proceeds with minimal waste formation and excellent incorporation of reactant atoms into the product, closely approaching the ideal values. This highlights not only the efficiency of the MgO@EDTA@Ag nanocatalyst but also its alignment with the principles of green and sustainable chemistry (Scheme 2).

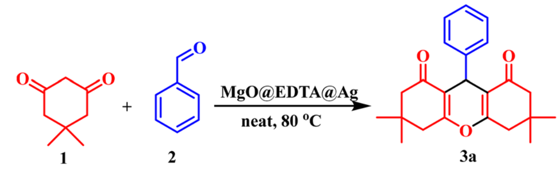

FW	140.17 g/mol	106.12 g/mol	350.45 g/mol
mmol	1 mmol	0.5 mmol	0.45 mmol
Amount	140 mg	0.05 mL	157 mg

Scheme 2 Green matrices for xanthene.

***E*-factor:**

The ideal value of the *E*-factor is zero.

E-factor = [total mass of raw materials − the total mass of product]/mass of the product.

E-factor of **3a** = [246 − 157]/157 = 0.23

Process mass intensity (PMI):

PMI = $\sum$(mass of stoichiometric reactants)/(mass of product)

= (140 + 53)/157 = 1.23

Reaction mass efficiency (RME):

RME = [mass of the desired product/$\sum$(molecular mass of reactants)] × 100

= [175/(140 + 53)] × 100 = 90.06%

Carbon efficiency (CE):

CE denotes the percentage of carbon in the reactants that remain in the product.

CE = [amount of carbon in product/total carbon present in reactants] × 100

= [no. of moles of product × no. of carbons in product/(moles of 1 × carbons in 1 + moles of 2 × carbons in 2)] × 100

= [(0.45 × 23)/(1 × 8 + 0.5 × 7)] × 100

= 0.90 × 100

= 90%

Table 3 shows the green metrics of our catalyst system, highlighting the efficiency and environmental compatibility of our method.

The photocatalytic assay

The photocatalytic activity of the synthesized MgO@EDTA@Ag nanocomposite was evaluated for the degradation of rhodamine B (RhB) under UV light irradiation. Rhodamine B is a prominent pollutant found in wastewater from the textile and food processing industries.[48] In this study, a time-dependent decline in the absorption spectra of RhB ($\lambda_{\max}$ = 554 nm) was

Table 3 Green metrics for the synthesis of **3a** using MgO@EDTA@Ag

Catalyst	*E*-factor	Process mass intensity (PMI)	Reaction mass efficiency (RME) (%)	Carbon efficiency (CE) (%)
MgO@EDTA@Ag	0.23	1.23	90.06	90

recorded to monitor photocatalytic degradation in the presence of the synthesized catalyst under UV light. The characteristic absorption peak at 554 nm assessed the degradation process. As shown in Fig. 15c, a significant decrease in the absorption intensity was observed with increasing UV exposure time from 0 to 60 minutes in the presence of the nanocomposite, indicating effective degradation of RhB. In contrast, no significant change in absorbance was observed in the absence of the catalyst, confirming the crucial role of the MgO@EDTA@Ag nanocomposite in the photocatalytic process. For the time-dependent experiment, 0.8 μM RhB solution was used. To this, 100 μL of the nanoparticle suspension (having a concentration of 0.2 mg mL^{-1}) was added to 2 mL of dye solution. This corresponds to the addition of 0.02 mg of nanocatalyst (100 μL × 0.2 mg mL^{-1} = 0.02 mg). The degradation efficiency of the catalyst reached 96% within 60 minutes, as evidenced by the fading of the pink colouration of the RhB solution and the near disappearance of the absorption peak. In comparison, $AgNO_3$ (Fig. 15a) and MgO (Fig. 15b) used individually under identical conditions showed significantly lower degradation efficiencies of 14.3% and 9.5%, respectively. The degradation efficiencies were calculated using the equation below,

$$\%\text{Degradation} = \left(\frac{A_0 - A_t}{A_0}\right) \times 100$$

where A_0 and A_t are the absorbance values before and after degradation,[49] respectively.

These results demonstrate that the MgO@EDTA@Ag nanocomposite effectively promotes the degradation of rhodamine B under UV radiation, with a notable decrease in dye concentration observed within a short exposure time.

Fig. 16a shows the time-dependent variation of normalized RhB concentration (C/C_0) under UV irradiation. The MgO@EDTA@Ag nanocomposite exhibits a rapid and continuous decrease in C/C_0, achieving near-complete degradation within 60 min, whereas

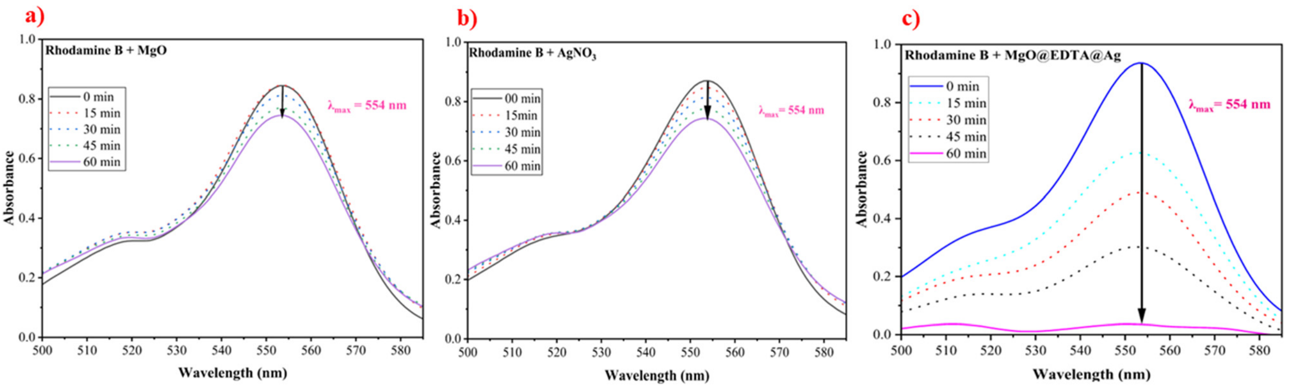

Fig. 15 Time-dependent degradation of RhB dye in the presence of a photocatalyst under UV light irradiation in the presence of (a) $AgNO_3$, (b) MgO, and (c) MgO@EDTA@Ag.

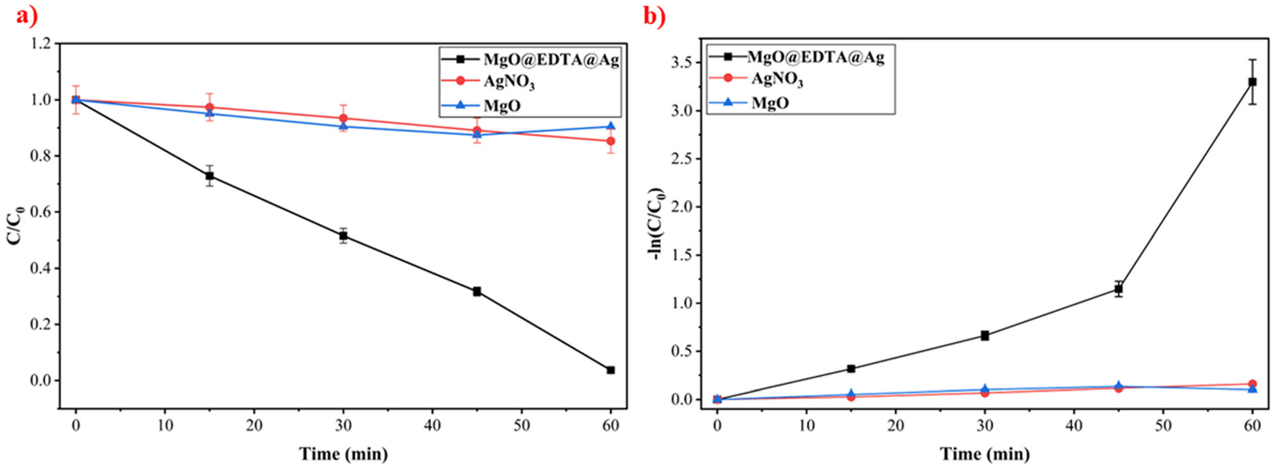

Fig. 16 The plot of (a) C/C_0 *vs.* time and (b) $-\ln C/C_0$ *vs.* time using different photocatalysts (MgO@EDTA@Ag, $AgNO_3$, MgO) for the degradation of rhodamine B dye.

$AgNO_3$ and MgO show negligible changes, indicating poor photocatalytic activity. The error bars represent standard deviations from repeated experiments, confirming good reproducibility. Fig. 16b presents the pseudo-first-order kinetic plot of $-\ln(C/C_0)$ *versus* time, where a linear trend is observed for MgO@EDTA@Ag, confirming pseudo-first-order behavior with a significantly higher apparent rate constant compared to MgO and $AgNO_3$. The intercept of the $\ln(C_0/C)$ *versus* time plot is approximately zero, confirming negligible initial adsorption and validating the pseudo-first-order kinetic assumption.

Conclusion

In this work, a MgO@EDTA@Ag nanocomposite was successfully synthesised and its effectiveness as a versatile catalyst for both organic transformations and environmental applications was demonstrated. It showed excellent catalytic activity in the solvent-free synthesis of xanthene derivatives, delivering high yields under neat conditions and maintaining its performance over multiple cycles. The material also exhibited strong photocatalytic efficiency, achieving up to 96% degradation of rhodamine B dye under UV light within 1 hour. A gradual increase in catalyst loading further improves the degradation rate, highlighting the role of catalyst concentration. Additionally, green chemistry metrics such as *E*-factor (0.23), process mass intensity (1.23), reaction mass efficiency (90.06%), and carbon efficiency (90%) demonstrated the environmental sustainability of the process, with values closely aligned with the ideal benchmark. Overall, the MgO@EDTA@Ag nanocomposite presents a promising, eco-friendly solution for both green chemical synthesis and wastewater treatment.

Although the present methodology is environmentally benign due to its solvent-free conditions, high atom economy, and catalyst reusability, the potential environmental impact associated with silver-based catalysts warrants further investigation. Future studies will focus on quantitative Ag leaching analysis under real wastewater conditions and ecotoxicity assessments to comprehensively evaluate the long-term sustainability and environmental safety of the MgO@EDTA@Ag nanocatalyst.

Conflicts of interest

The authors declare no conflicts of interest.

Data availability

The authors declare that all the data in this manuscript are available upon request.

Supplementary information (SI): the ^1H NMR, ^{13}C NMR, and mass spectrometry data of the xanthene derivatives, and the XRD and SEM data of the recycled catalyst. See DOI: https://doi.org/10.1039/d5ma01226k.

Acknowledgements

S. S., A. Brahma, and A. Borah, are thankful to the Department of Chemistry and Institute for Nanomedical Sciences (INMS), University of Delhi, for providing infrastructure. S. S. and A. Brahma are also thankful to USIC for providing instrumentation facilities. A. Brahma (Grant No. 231610191350) and A. Borah (Grant No. 231620214515) are thankful to UGC-JRF for providing them with financial assistance.

References

1 S. Mondal, B. Pramanik, R. Sahoo and M. C. Das, A Chemically Robust 2D Ni-MOF as an Efficient Heterogeneous Catalyst for One-Pot Synthesis of Therapeutic and Bioactive 2-Amino-3-Cyano-4*H*-Pyran Derivatives, *ChemSusChem*, 2025, **18**, e202401248.

2 P. Bernard, P. Stelmachowski, P. Bros, W. Makowski and A. Kotarba, Demonstration of the influence of specific surface area on reaction rate in heterogeneous catalysis, *J. Chem. Educ.*, 2021, **98**, 935–940.

3 J. S. Bates and R. Gounder, Chemical kinetics of heterogeneous catalysis: experimental research methodologies and case studies of site-isolated materials, *Catal. Rev.*, 2025, 1–47.

4 A. Brahma, A. Borah, Y. Sharma, J. Sperry, R. Chandra and S. Singh, Novel $CuFe_2O_4$@ agar@ Cu_2O Nanocatalyst for Sustainable Synthesis of Biologically Active 1, 4-Benzodiazepines and 1-Aryl-1 H-tetrazoles, *ACS Sustainable Chem. Eng.*, 2025, **13**(32), 12853–12864.

5 K. A. M. Ahmed, Efficient removal of phenol pollutants with CuO nanorods and nanoparticles as a reusable heterogeneous catalysts, *Appl. Phys. A*, 2025, **131**, 1–10.

6 S. Kohli, K. Aggarwal, S. Singh, N. Sharma and R. Chandra, CuI/MnO_2 nanocatalysed synthesis of bioactive 2-substituted benzimidazoles, *Inorg. Chem. Commun.*, 2025, **171**, 113556.

7 S. Ghotekar, D. Sanap, K. Y. A. Lin, H. Louis, D. Pore and R. Oza, A novel green synthesis of honey-mediated $CoCr_2O_4$ nanoparticles and their expeditious heterogeneous catalytic role for the synthesis of 5-aryl-[1,2,4] triazolidine-3-thiones, *Res. Chem. Intermed.*, 2024, **50**, 49–68.

8 K. Aggarwal, A. Brahma, Y. Sharma, P. Rajput, B. Sachdeva, A. Singh and S. Singh, Recent progress in copper nanomaterials: catalysis, energy, biomedicine, and environmental applications, *Mater. Adv.*, 2025, **6**, 9296–9339.

9 M. Maia, D. I. Resende, F. Duraes, M. M. Pinto and E. Sousa, Xanthenes in Medicinal Chemistry–Synthetic strategies and biological activities, *Eur. J. Med. Chem.*, 2021, **210**, 113085.

10 A. Ebadi, A. Karimi, A. Bahmani, Z. Najafi and G. Chehardoli, Novel Xanthene-1, 8-dione Derivatives Containing the Benzylic Ether Tail as Potent Cytotoxic Agents: Design, Synthesis, In Vitro, and In Silico Studies, *J. Chem.*, 2024, **1**, 6612503.

11 J. J. Omolo, M. M. Johnson, S. F. Van Vuuren and C. B. De Koning, The synthesis of xanthones, xanthenediones, and

spirobenzofurans: their antibacterial and antifungal activity, *Bioorg. Med. Chem. Lett.*, 2011, **21**(23), 7085–7088.

12 T. Librowski, R. Czarnecki, T. Czekaj and H. Marona, New xanthone derivatives as potent anti-inflammatory agents, *Medicina*, 2005, **41**(1), 54–58.

13 M. Abualhasan, M. Hawash, S. Aqel, M. Al-Masri, A. Mousa and L. Issa, Biological evaluation of xanthene and thioxanthene derivatives as antioxidant, anticancer, and COX inhibitors, *ACS Omega*, 2023, **8**(41), 38597–38606.

14 Y. B. S. Tanwer, S. Watre Sangma, S. R. Patra, K. Swain, S. Bhunia, S. Pal and D. Das, Water Extract of Red Mud, a Renewable Aqueous Medium for the Synthesis of Functionalized Xanthene Derivatives via a One-Pot Three-Component Reaction: Mechanistic Studies and Reaction Scope, *ACS Sustainable Resour. Manage.*, 2025, **2**, 492–500.

15 S. Khandelwal, Y. K. Tailor, E. Rushell and M. Kumar, Use of sustainable organic transformations in the construction of heterocyclic scaffolds, *Green Approaches in Medicinal Chemistry for Sustainable Drug Design*, 2020, pp. 245–352.

16 P. Bansal, G. R. Chaudhary, N. Kaur and S. K. Mehta, An efficient and green synthesis of xanthene derivatives using CuS quantum dots as a heterogeneous and reusable catalyst under solvent free conditions, *RSC Adv.*, 2015, **5**, 8205–8209.

17 A. J. Wein and M. L. Moy, Drug treatment of urinary incontinence in women, *Female Urology E-Book: Text with DVD*, 2002, vol. 3, pp. 233–256.

18 N. Cusick and H. Schönherr, Phloxine B-loaded polymersomes enable eradication of Pseudomonas aeruginosa and Staphylococcus aureus in antimicrobial photodynamic therapy, *RSC Adv.*, 2025, **15**(24), 18815–18825.

19 M. Houdi, S. Kapur, B. Chamma, K. Sidhu, E. Wolinsky, P. Kancharla and C. G. Burkhart, Anticholinergic Treatments for Focal and Generalized Hyperhidrosis, *JAAD Rev.*, 2025, **5**, 110–120.

20 S. Khan, T. Noor, N. Iqbal and L. Yaqoob, Photocatalytic dye degradation from textile wastewater: a review, *ACS Omega*, 2024, **9**, 21751–21767.

21 Y. Lu, Y. Zhang, J. Zhang, Z. Li, F. Hu, D. Pan and Q. Shao, Electrochemically synthesized Tin micro-nanometer powders for visible light photocatalytic degradation of rhodamine B dye from polluted water, *Adv. Compos. Hybrid Mater.*, 2024, **7**, 110.

22 N. Kuruthukulangara and I. V. Asharani, Photocatalytic degradation of rhodamine B, a carcinogenic pollutant, by MgO nanoparticles, *Inorg. Chem. Commun.*, 2024, **160**, 111873.

23 Y. Li, J. Song, X. Zhao, B. Li, Z. Wang, J. Yang and Y. Cong, Ag Nanoparticles Supported on h-BN/BiPO4 Heterostructures as a Photocatalyst for the Degradation of rhodamine B, *ACS Appl. Nano Mater.*, 2024, **7**, 9116–9125.

24 B. Sachdeva, K. Aggarwal, A. Singh, K. Kumari, R. Chandra and S. Singh, Advancements in silver-based nanocatalysts for organic transformations and other applications: a comprehensive review (2019–2024), *RSC Adv.*, 2025, **15**, 17591–17634.

25 P. Yadav, R. Saini and A. Bhaduri, Facile synthesis of MgO nanoparticles for effective degradation of organic dyes, *Environ. Sci. Pollut. Res.*, 2023, **30**, 71439–71453.

26 P. Yadav, R. Saini and A. Bhaduri, Facile synthesis of MgO nanoparticles for effective degradation of organic dyes, *Environ. Sci. Pollut. Res.*, 2023, **30**, 71439–71453.

27 P. Yadav, R. Saini and A. Bhaduri, Facile synthesis of MgO nanoparticles for effective degradation of organic dyes, *Environ. Sci. Pollut. Res.*, 2023, **30**, 71439–71453.

28 S. Ali, H. Zahra, M. U. Ahmad, A. A. Abdel-Rheem, M. Afzaal, R. Nawaz and Y. A. Bin Jardan, Synergistic photocatalytic and biomedical applications of Ag_2O-immobilized Bacillus subtilis-hyaluronic acid, *Microb. Cell Fact.*, 2025, **24**, 1–17.

29 A. Behnami, J. P. Croué, E. Aghayani and M. Pourakbar, A catalytic ozonation process using MgO/persulfate for degradation of cyanide in industrial wastewater: mechanistic interpretation, kinetics and by-products, *RSC Adv.*, 2021, **11**, 36965–36977.

30 Y. Liu, M. Chen and H. Yongmei, Study on the adsorption of Cu(II) by EDTA functionalized Fe_3O_4 magnetic nanoparticles, *Chem. Eng. J.*, 2013, **218**, 46–54.

31 S. Kohli, G. Rathee, S. Hooda and R. Chandra, An efficient approach for the green synthesis of biologically active 2,3-dihydroquinazolin-4(1*H*)-ones using a magnetic EDTA coated copper based nanocomposite, *RSC Adv.*, 2023, **13**, 1923–1932.

32 N. Bao, X. Miao, X. Hu, Q. Zhang, X. Jie and X. Zheng, Novel synthesis of plasmonic Ag/AgCl@TiO_2 continues fibers with enhanced broadband photocatalytic performance, *Catalysts*, 2017, **7**, 117.

33 N. Algethami, A. Rajeh, H. M. Ragab, A. E. Tarabiah and F. Gami, Characterization, optical, and electrical properties of chitosan/polyacrylamide blend doped silver nanoparticles, *J. Mater. Sci.: Mater. Electron.*, 2022, **33**, 10645–10656.

34 I. K. Kgosiemang, R. Lefojane, P. Direko, Z. Madlanga, S. Mashele and M. Sekhoacha, Green synthesis of magnesium and cobalt oxide nanoparticles using Euphorbia tirucalli: Characterization and potential application for breast cancer inhibition, *Inorg. Nano-Met. Chem.*, 2020, **50**, 1070–1080.

35 A. I. Quilez-Molina, S. Barroso-Solares, M. Á. Rodríguez-Pérez and J. Pinto, Toward a Green Chemistry Approach for the Functionalization of Melamine Foams with Silver Nanoparticles, *Macromol. Mater. Eng.*, 2023, **308**, 2300178.

36 H. Singh, A. Kachore, V. Aggarwal, E. Bala, Saima, R. Kumar and P. K. Verma, Magnetically Separable and Reusable Fe_3O_4 Nanoparticles for Reduction of Nitroarenes in Water, *ChemistrySelect*, 2025, **10**, e202501004.

37 H. Labhade, J. Wable and A. Kategaonkar, Efficient Ce-doped MgO@Ag core-shell catalyst for green synthesis of xanthenes, *Res. Chem. Intermed.*, 2025, **51**, 5779–5807.

38 K. A. Shaikh and U. N. Chaudhar, Facile and Efficient Synthesis of Xanthene Derivatives Mediated by Lanthanum(III) Nitrate Hexahydrate under Solvent Free Conditions, *Chem. J. Mold.*, 2020, **15**, 99–104.

39 S. Karmakar, P. Das, D. Ray, S. Ghosh and S. K. Chattopadhyay, Ag(I)-Catalyzed domino cyclization–addition sequence with simultaneous carbonyl and alkyne

activation as a route to 2, 2′-disubstituted bisindolylarylmethanes, *Org. Lett.*, 2016, **18**, 5200–5203.

40 D. Fan, X. Dong, Y. Yu and M. Zhang, A DFT study on the aldol condensation reaction on MgO in the process of ethanol to 1,3-butadiene: understanding the structure–activity relationship, *Phys. Chem. Chem. Phys.*, 2017, **19**, 25671–25682.

41 P. Yadav, R. Saini and A. Bhaduri, Facile synthesis of MgO nanoparticles for effective degradation of organic dyes, *Environ. Sci. Pollut. Res.*, 2023, **30**, 71439–71453.

42 S. Kohli, G. Rathee, S. Hooda and R. Chandra, An efficient approach for the green synthesis of biologically active 2,3-dihydroquinazolin-4(1*H*)-ones using a magnetic EDTA coated copper based nanocomposite, *RSC Adv.*, 2023, **13**, 1923–1932.

43 S. Singh, T. Goel, A. Singh, H. Chugh, N. Chakraborty, I. Roy, M. Tiwari and R. Chandra, Synthesis and characterization of Fe_3O_4@SiO_2@PDA@Ag core–shell nanoparticles and biological application on human lung cancer cell line and antibacterial strains, *Artif. Cells, Nanomed., Biotechnol.*, 2024, **52**, 46–58.

44 L. Moradi and M. Mirzaei, Immobilization of Lewis acidic ionic liquid on perlite nanoparticle surfaces as a highly efficient solid acid catalyst for the solvent-free synthesis of xanthene derivatives, *RSC Adv.*, 2019, **9**, 19940–19948.

45 H. Singh, Himanshu, A. Kachore, V. Aggarwal, E. Bala, Saima and P. K. Verma, Iron-based heterogenous nanocatalyst from Taraxacum officinale for Hantzsch, Knoevenagel, and Biginelli reactions, *Langmuir*, 2025, **41**, 23163–23181.

46 M. A. Taheri, M. Setoodehkhah and M. Moradian, Sulfonated Schiff base immobilized on magnetite-chitosan as an efficient nanocatalyst for the synthesis of xanthene derivatives, *Sci. Rep.*, 2025, **15**, 19056.

47 A. Katsumiti, D. Gilliland, I. Arostegui and M. P. Cajaraville, Mechanisms of toxicity of Ag nanoparticles in comparison to bulk and ionic Ag on mussel hemocytes and gill cells, Cajaraville, *PLoS One*, 2015, **10**(6), e0129039.

48 L. T. Nguyen, D. V. N. Vo, L. T. Nguyen, A. T. Duong, H. Q. Nguyen, N. M. Chu and T. Van Tran, Synthesis, characterization, and application of $ZnFe_2O_4$@ ZnO nanoparticles for photocatalytic degradation of rhodamine B under visible-light illumination, *Environ. Technol. Innovation*, 2022, **25**, 102130.

49 M. H. Ashfaq, M. Imran, A. Haider, A. Shahzadi, M. Mustajab, A. Ul-Hamid and M. Ikram, Antimicrobial potential and rhodamine B dye degradation using graphitic carbon nitride and polyvinylpyrrolidone doped bismuth tungstate supported with in silico molecular docking studies, *Sci. Rep.*, 2023, **13**, 17847.